Electronic Journal of Structural Engineering

Original Article

Cite this: DOI:10.56748/ejse.26830

Received Date: 20 May 2025
Accepted Date: 07 April 2026

1443-9255
https://ejsei.com/ejse

Seismic performance of a prefabricated concrete frame node

Shufeng Li [a b], Di Zhao [a*], Can Song [a], Ke Xu [a], Zijun Guo [a], Hangdong Ma [a], Panpan Wu [a]

[a] School of Civil Engineering, Xuchang University, Xuchang, 461000, China
[b] Henan Province Engineering Technology Research Center for Ecological and High-quality Utilization of Construction Solid Waste, Xuchang, 461000, China
*Corresponding author: zhaohy1978321@yeah.net

Abstract

The bolt end plate connection used in steel structures and composite structures has been extended to concrete, forming a through core high-strength bolt connection assembled concrete frame structure. To study the seismic performance and failure mode of the structure, the finite element software is used to simulate low cycle repeated loading tests of the node. Modeling analysis is carried out with axial compression ratio, concrete strength grade, end plate thickness, and other main variable parameters. The influence of different influencing factors on the seismic performance of the node is also explored. The results indicate that the ductility coefficient of the node is generally between 2.43 and 4.16, overall greater than 3.0, demonstrating good ductility and deformation capacity. When the node fails, the equivalent viscous damping coefficient is between 0.3-0.4, demonstrating good energy dissipation capacity. In addition, increasing the thickness of the end plate can significantly improve the stiffness of the node, optimize the efficiency of moment transmission, and suppress adverse deformation. Stress analysis shows that the force transmission of each component of the node is uniform, and key components such as end plates and high-strength bolts are subjected to reasonable forces. The node realizes the design criterion of "strong column, weak beam, stronger node", and the plastic hinge at the beam end is fully developed.

Keywords

Prefabricated concrete, Seismic performance, Deformation, Energy dissipation, Mechanical properties

1. Introduction

China has entered a critical period of achieving the dual carbon target. Due to their unique advantages, prefabricated buildings have become the main means of construction to achieve the dual carbon target. Therefore, new structural systems with good seismic performance, convenient construction, and good post-earthquake recovery are of great significance. Concrete frame structures still dominate in Chinese architecture. There has been some research on new structural systems of prefabricated concrete frames. Nzabonimpa et al. (2018) proposed a new type of steel-concrete composite beam-column joint connected by high-strength bolts and proved that the joint has good seismic performance through low cyclic loading experiments. The 6-bolt extended multiple-row moment end-plate connections with reinforced PJP welds were tested to investigate the strength of the connection and the reinforced PJP weld used on the connection. The results show that proper design of PJP welds can be effectively used in flange to end-plate connections of beam to column connections (Ramseyer and Sherry, 2019). Elflah et al. (2019a, b) conducted a series of experimental tests on twelve single-sided austenitic stainless-steel beam-to-column joints, including four types of configurations: flush and extended end-plate connections, top and seat angle cleat connections, and top, seat and double web cleat connections, which were further used to verify the developed FE models. Zhang et al. (2020) proposed a new square steel tube concrete column steel beam joint with double T-shaped steel core bolt connection, which is easy to assemble and can be replaced after earthquakes. A full-scale finite element analysis model was established using the finite element analysis software ABAQUS to conduct refined numerical simulations under low cycle reciprocating loads. The influence of the thickness of the T-shaped steel flange, web plate, and shear plate on the hysteresis performance of the joint was studied. The results showed that the joint has good strength, stiffness, and energy dissipation capacity, and can meet the seismic design goal of "strong node, weak component". Wu et al. (2022) proposed an assembled bolt connection node form, which involves inserting steel beams between the upper and lower outer ring plates, and connecting the steel beam flanges to the inclined straight edge ring plates using high-strength bolts. In this way, the force transmission path at the node connection can be changed to the stress performance of the ring plates can be improved. Three quasi-static loading tests were conducted on the edge column nodes, and the results showed that the equivalent viscous damping coefficients of the three specimens were 0.320, 0.355, and 0.283, respectively. This indicates that the node has good energy dissipation capacity. The plastic hinge of the specimen beam with flange cover plate appears on the beam section outside the ring plate range, while the plastic hinge of the specimen beam without flange cover plate appears on the beam section outside the outermost row of bolts. Wu et al. (2020a, b) proposed a reliable dry connection method, namely a new modular precast SRC column steel beam composite joint (MPCJ), to study the seismic performance of beam column joints in prefabricated frame structures. Based on this, three different types of beam column joints (bolted welded hybrid connection, bolted connection, and welded connection) were proposed and subjected to low cycle reciprocating load tests and finite element analysis. Under all three different connection methods, beam-end bending failure occurred, and the hysteresis curve was stable and full. The ductility coefficient and equivalent viscous damping coefficient of the three joints were greater than 4 and 0.2, respectively, meeting the seismic performance requirements. Based on experimental results and numerical verification, simplified equations for bending and shear bearing capacity were proposed. Bao et al. (2023a, b, 2025) explored the seismic performance of precast concrete piers with different connection forms, as well as the performance degradation laws under the coupled effects of freeze-thaw, chloride salt, and wetting-drying in cold regions through quasi-static tests, artificial climate environment simulations, and finite element analysis. The results showed that the yield load and peak load of piers with grouted splice sleeve connections could reach 101.9% and 95.7% of those of cast-in-place structures respectively. Their seismic performance was close to that of CIP structures. The unbonded post-tensioned piers have excellent self-centering ability, with a residual displacement of less than 7 mm. The increase in prestress could enhance their load-bearing capacity and stiffness. The coupled effects of the cold-region environment reduced the peak load of the piers by 8.4% and the ultimate displacement by 15.3%. A load-bearing capacity reduction factor of 0.85 was recommended for 200 freeze-thaw cycles. Both types of precast piers were suitable for moderate-to-low seismic intensity zones (≤ VIII), and the connection durability needed to be optimized for high-seismic intensity zones. In addition, the established finite element model could effectively predict their seismic response. Based on the above analysis, a prefabricated concrete frame node with high-strength bolt end plate connection is proposed to study the seismic performance of the node, and the finite element software is used to simulate its quasi-static test.

2. Selection of relevant parameters for finite element analysis

2.1 The constitutive model of steel

The steel use is Q345 steel, and the constitutive simplification of the steel is divided into three stages (Nejati et al., 2019): elastic stage, strengthening stage, and failure stage. The corresponding yield strength f_y =345 MPa, ultimate strengthf_u =470 MPa, elastic

modulus$E$ =2.06×10⁶ MPa, and Poisson ratio v = 0.3.The bolt adopts HTH1080 horizontal and trilinear constitutive models (Hassan et al., 2024; Tekieh et al., 2022), with a yield strength of 1080 MPa and an ultimate strength of 1250 MPa, respectively.

2.2 The constitutive model of steel bars

Considering the hysteresis performance when steel bars and concrete work together, rather than steel bars work alone, the steel bar hysteresis model of the RC structure (reinforced concrete construction) developed by Fang et al. (2018) is applied. There are three input parameters for the material: (MPa), (MPa), and (ratio of hardening stiffness to initial stiffness) (Zhelyazov and Thorhallsson, 2022). The specific data of the materials are shown in Table 1.

Table 1. Reinforcement parameters

Reinforcement parameters	E_s (MPa)	f_y (MPa)	E_{Sh}/E_s
HRB400	200000	400	0.001
HRB1080	200000	1080	0.001
HRB1100	200000	1100	0.001
HTH1080	200000	1080	0.001

where, $E_s$is the elastic modulus, f_y is the yield strength, and $E_{Sh}/E_s$is the ratio of hardening stiffness to initial stiffness.

2.3 The constitutive model of concrete

The plastic damage model of concrete adopts the default value in ABAQUS. In the elastic stage, the stress-strain relationship can be obtained according to the elastic modulus of the material. In the plastic stage, the stress-strain relationship of concrete needs to be calculated and analyzed according to the model proposed by Code for design of concrete structures (GB/50010-2010) (2010). The parameters are shown in Table 2 and Table 3. The values of concrete plastic parameters in the concrete plastic damage model are shown in Table 4.

Table 2. Parameter selection of concrete uniaxial tensile stress-strain curve

$f_{t,r}(N/mm^2)$	1.0	1.5	2.0	2.5	3.0	3.5	4.0
$\varepsilon_{t,r}(10^{-6})$	65	81	95	107	118	128	137
α_t	0.31	0.70	1.25	1.95	2.81	3.82	5.00

where, $f_{t,r}$ is the representative value of tensile strength; $\varepsilon_{t,r}$is the tensile strain corresponding to$f_{t,r}$; $\alpha_t$is the parameter of concrete falling section under uniaxial tension.

Table 3. Parameter selection of stress-strain curve of concrete under uniaxial compression

$f_{c,r}(N/mm^2)$	20	25	30	35	40	45	50	55	60
$\varepsilon_{c,r}(10^{-6})$	1470	1560	1640	1720	1790	1850	1980	1920	2030
a_c	0.74	1.06	1.36	1.65	1.94	2.21	2.48	2.74	3.00
$\varepsilon/\varepsilon_{c,r}$	3.0	2.6	2.3	2.1	2.0	1.9	1.8	1.8	1.8

where,$f_{c,r}$ is the representative value of compressive strength; $\varepsilon_{c,r}$ is the compressive strain corresponding to $f_{c,r}$; $a_c$is the parameter of concrete falling section under uniaxial compression.

Table 4. Values of plastic parameters of concrete in ABAQUS

Expansion angle	Eccentricity	f_{b0}/f_{c0}	K	Stickiness parameter
38°	0.1	1.16	0.667	0.005

2.4 Mesh Generation

The selection of grid size is mainly based on the force characteristics of the structure. The global element size for the grid division of each component is 100 mm. Due to the complex stress in the connection area of the node core, the mesh size is adjusted to 20 mm. The grid division of the nodes and various components is shown in Fig. 1.

2.5 Comparison of damage modes

The damage of finite element simulation and testing are shown in Fig.2. The testing of beam column joints generates plastic hinges at the end of the beam, and the concrete in the plastic hinge area fractures locally. According to the results of the finite element modeling, the damage is essentially the same with the test, and the damage at the beam end is the most severe.

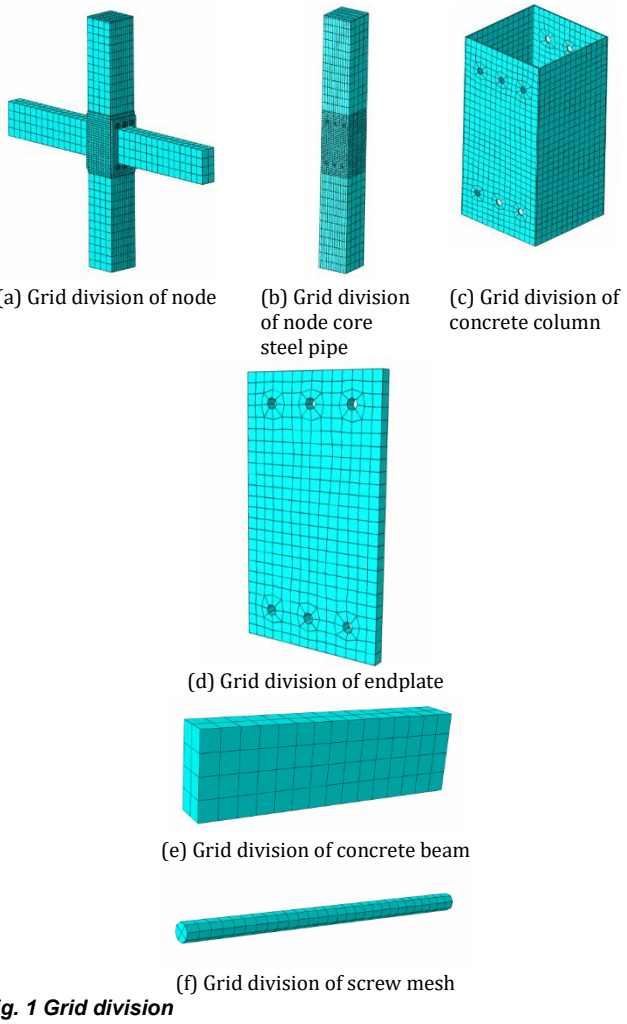

(a) Grid division of node (b) Grid division of node core steel pipe (c) Grid division of concrete column

(d) Grid division of endplate

(e) Grid division of concrete beam

(f) Grid division of screw mesh

Fig. 1 Grid division

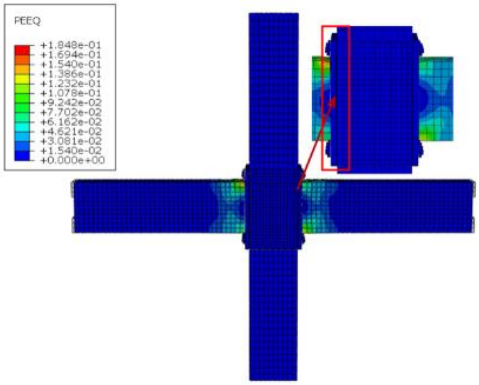

(a) Simulated failure in the nodal core area

(b) Experimental failure in the nodal core area (The photograph was taken by the authors in Xian, China, on June 20, 2016)

Fig. 2 Comparison of failure in the nodal core area

3. Seismic performance of nodes

3.1 Geometric features of nodes

The dimensions of the node entity model are shown in Fig. 3, and the node reinforcement is shown in Fig. 4. The basic parameters of the test piece are shown in Table 5. The determination of this parameter is mainly based on the results of previous experiments and preliminary analysis of the model.

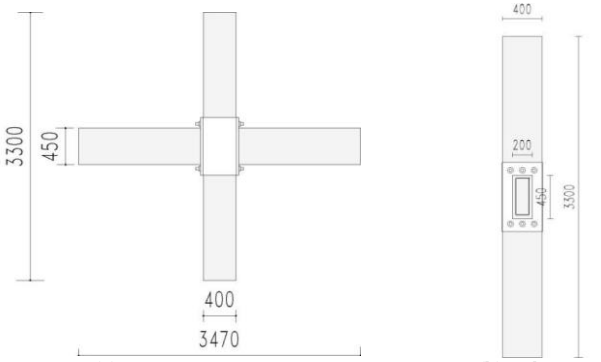

(a) Front view (b) Side view

(c) Vertical view

Fig. 3 Node size diagram

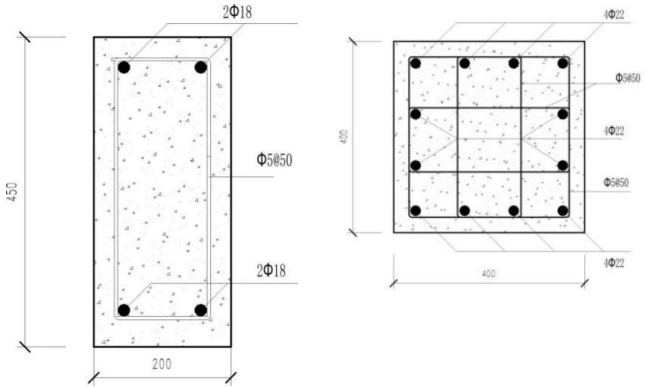

(a) Detailed drawing of beam reinforcement (b) Detailed drawing of column reinforcement

Fig. 4 Reinforcement diagram of beams and columns

Table 5. Basic parameters of each specimen

Nodes	Axial compression ratio	Concrete strength	Bolt preload	End-plate thickness
PAN-01	0.3	C30	200kN	30mm
PAN-02	0.3	C50	200kN	30mm
PAN-03	0.3	C40	300kN	30mm
PAN-04	0.3	C40	400kN	30mm
PAN-05	0.3	C40	200kN	20mm
PAN-06	0.3	C40	200kN	40mm
PAN-07	0.3	C40	200kN	30mm
PAN-08	0.5	C40	200kN	30mm
PAN-09	0.7	C40	200kN	30mm

3.2 Load displacement hysteresis curve

The load displacement curves of each specimen are shown in Fig. 5.

From Fig. 5, it can be seen that the hysteresis curves of each specimen are similar, basically between shuttle-shaped and bow-shaped. Before failure, all parts of the specimen are in the elastic stage, and the load displacement changes linearly. As large displacement increases, the load increases slowly and the stiffness decreases to a certain extent. However, under the same level of displacement control, the three cycle curves are basically similar, and the degradation of strength and stiffness is not significant. The concrete grades of specimens PAN-01, PAN-02, and PAN-07 are different. From the hysteresis curve, it can be seen that the strength of concrete affects the fullness of the curve. The higher the strength, the fuller the curve, but the later descending section will appear earlier (Rahnavard et al., 2020; Kalmykova, 2021). The pre-tightening force of bolts on specimens PAN-03, PAN-04, and PAN-07 are different. From the hysteresis curve, the pre-tightening force of bolts has little effect on the specimens, and the bearing capacity of the specimens is almost the same. The thickness of endplates of specimens PAN-05, PAN-06, and PAN-07 is different. It can be clearly seen from the hysteresis curve that the thickness of endplates has a significant impact on the specimens. Thin end-plate thickness specimens fail prematurely, while thick end-plate thickness specimens increase their ultimate bearing capacity. The main reason is that the increase in end plate stiffness will improve bending moment transmission and suppress adverse deformation. The axial compression ratios of specimens PAN-07, PAN-08, and PAN-09 are different. It can be clearly seen from the hysteresis curve that as the axial compression ratio increases, the fullness of the specimens decreases. The main reason is that under the premise that the axial compression ratio does not exceed the specification limit, moderately increasing the axial compression ratio can strengthen the constraint on the section of the component, suppress the early cracking of concrete, enhance the stress coordination between steel bars and concrete, delay the yield of longitudinal bars and the collapse process of concrete. It allows the component to withstand greater cyclic loads (increasing bearing capacity) and makes the yield energy dissipation of steel bars and the shear energy dissipation of concrete more sufficient (full hysteresis curve).

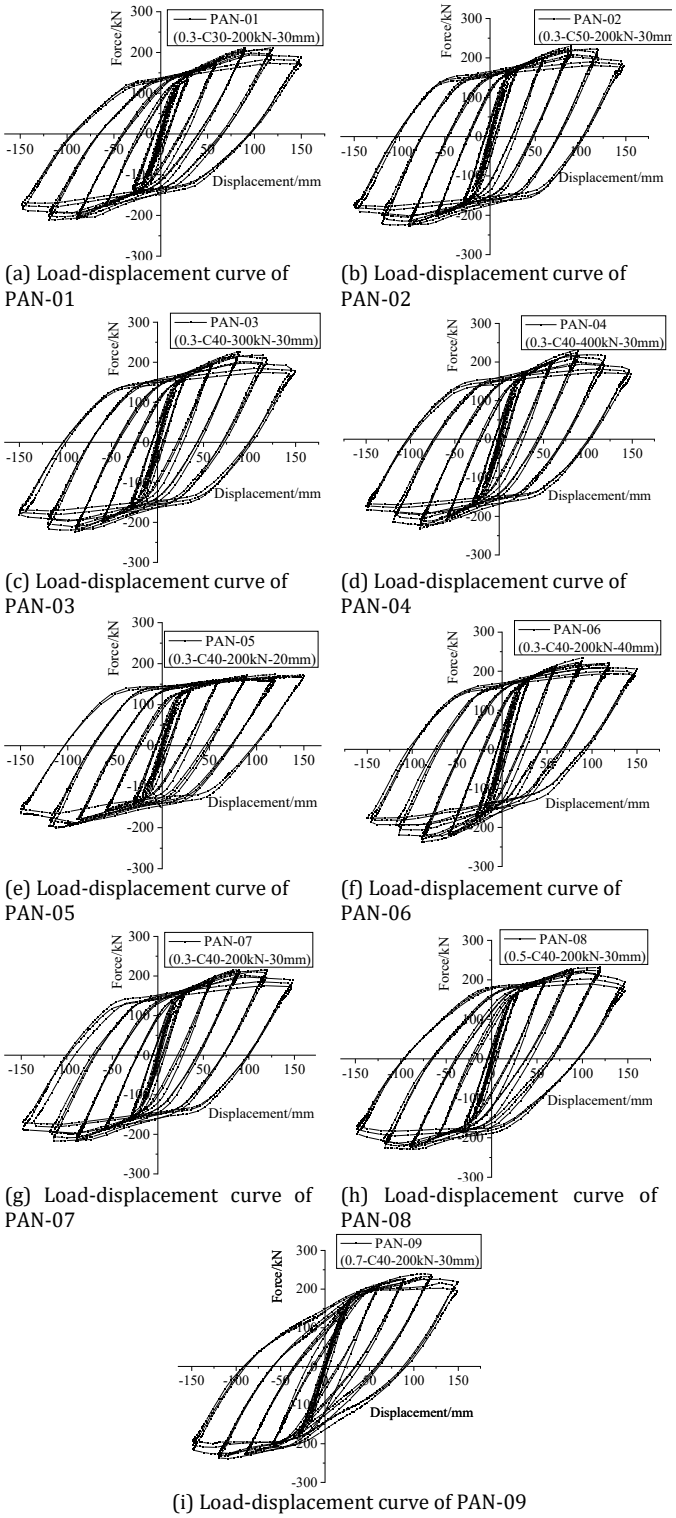

(a) Load-displacement curve of PAN-01

(b) Load-displacement curve of PAN-02

(c) Load-displacement curve of PAN-03

(d) Load-displacement curve of PAN-04

(e) Load-displacement curve of PAN-05

(f) Load-displacement curve of PAN-06

(g) Load-displacement curve of PAN-07

(h) Load-displacement curve of PAN-08

(i) Load-displacement curve of PAN-09

Fig. 5 Load displacement curves of each specimen

3.3 Skeleton curves

The load displacement curves of each specimen are shown on Fig. 6.

From Fig. 6, it can be seen that as the concrete strength grade increases, the yield load and ultimate load on the skeleton curve both increases, and the final decreasing trend is consistent. This indicates that concrete strength has a certain impact on the seismic performance of the specimen. As the pre-tightening force of the bolts increases, the skeleton curve is basically consistent, indicating that the specimen meets the specification requirements of applying pre-tightening force to the bolts (Al-Huri et al., 2023). There is no need to excessively increase the pre-tightening force of the bolts. When the thickness of the end plate is 20mm, the specimen fails prematurely and has a lower bearing capacity; when it changes from 20mm to 30mm, the yield load and ultimate load of the specimen are greatly increased; when it changes from 30mm to 40mm, compared with changing from 20mm to 30mm, the yield load and ultimate load of the specimen are increased, but not particularly significantly. Therefore, increasing the thickness of the end-plate within a certain range can greatly improve the bearing capacity of the structure.

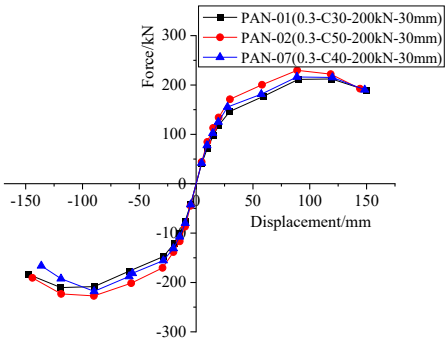

(a) Load displacement skeleton curve under different concrete grades

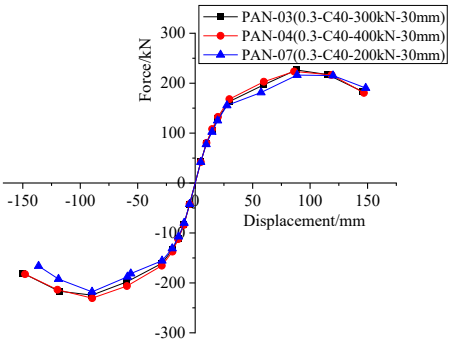

(b) Load displacement skeleton curve under different bolt pre tightening forces

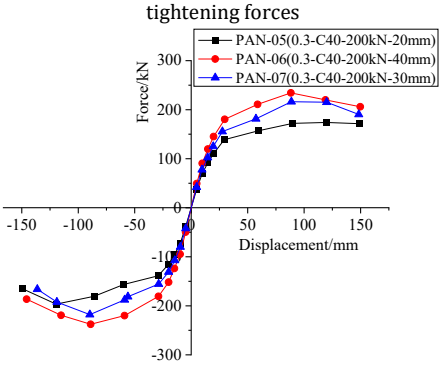

(c) Load displacement skeleton curves under different end plate thicknesses

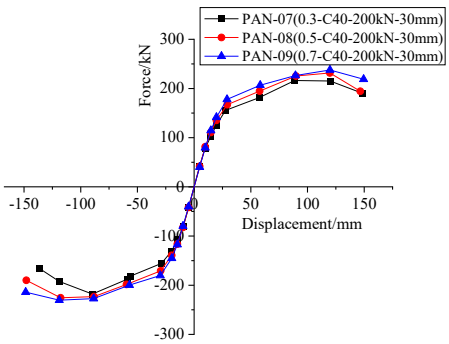

(d) Load displacement skeleton curves under different axial compression ratios

Fig. 6 Load displacement skeleton curve of each specimen

3.4 Stiffness degradation

The stiffness degradation curves of each specimen are shown in Fig. 7.

From Fig. 7, it can be seen that the variation of bolt preload has little effect on the stiffness degradation of the specimen, while the variation of end-plate thickness has the greatest impact on the stiffness degradation of the specimen. The variation of concrete grade and axial compression ratio has a moderate impact on the stiffness degradation of the specimen. In the initial stage of loading, the specimen is basically in the elastic stage, and the stiffness degradation is not significant. With the continuous increase of displacement, failure of the concrete beam continues to develop, and the development of plastic compressive stress at the top and bottom of the beam end plastic hinge reduces the structural response. At this stage, stiffness degradation is significant. After yielding, the failure of the specimen is basically stable state. Therefore, the stiffness degradation is slow at this stage. In the later stage of loading, there is no much difference in stiffness when performing three cycles per level. This indicates that the composite component has good resistance to deformation, and the resistance to deformation is relatively stable.

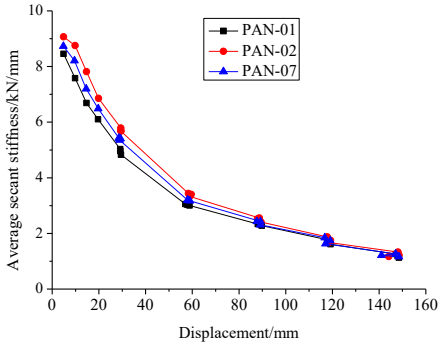

(a) Degradation of average secant stiffness under different concrete grades

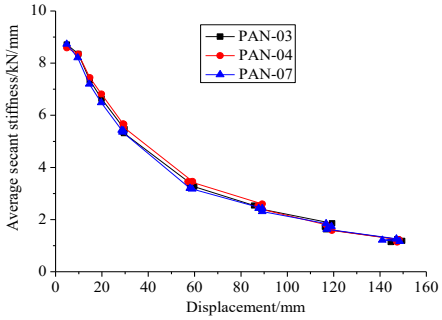

(b) Degradation of average tangent stiffness under different bolt pre tightening forces

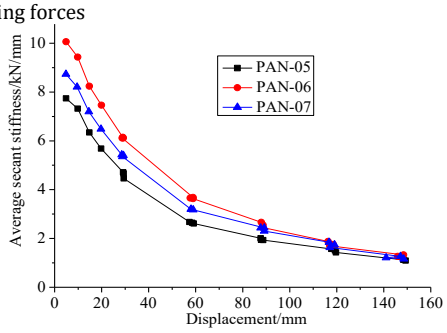

(c) Degradation of average secant stiffness at different end plate thicknesses

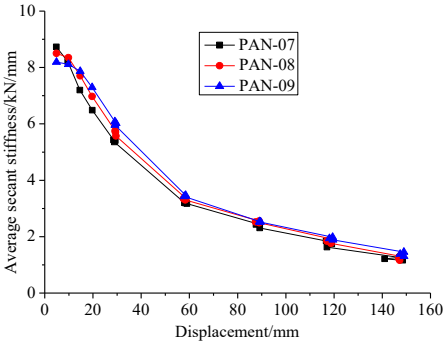

(d) Degradation of average secant stiffness under different axial compression ratios

Fig. 7 Degradation of average secant stiffness of specimens

3.5 Ductility coefficient

The ductility of specimens under different concrete strength grades, bolt pre-tightening forces, end-plate thicknesses, and axial compression ratios are shown in Tables 6-9.

From Tables 6-9, it can be seen that the ductility coefficient of this node is generally between 2.43 and 4.16, with an overall value greater than 3.0, indicating that the node has good ductility and deformation capacity, which meets the ductility design requirements of RC structures (Amer et al., 2025; Yeganeh and Hossain, 2023). Moreover, the ductility coefficient increases with the increase of concrete strength, bolt preload, end plate thickness, and axial compression ratio. The concrete strength grade, end plate thickness, and axial compression ratio have a greater impact on the ductility of this node, and the bolt preload has a certain improvement on the ductility of this node, but not significant.

3.6 Energy dissipation

The equivalent viscous damping coefficients of each specimen are shown in Fig. 8.

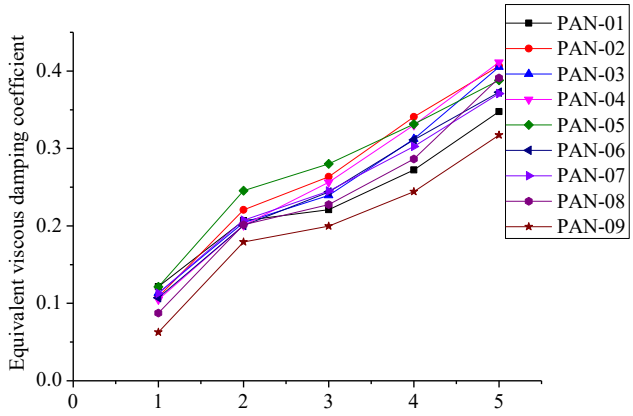

Fig. 8 Diagram of equivalent viscous damping coefficient

As shown in Fig. 8, the equivalent viscous damping coefficient of the assembled concrete frame node connected by the through core high-strength bolt is between 0.3 and 0.4 when it fails, demonstrating good energy dissipation capacity. The equivalent viscous damping coefficient is the highest when the nodes PAN-02 (C50), PAN-03 (300kN) and PAN-04 (400kN) fail, and that is the lowest when the nodes PAN-09 (axial compression ratio of 0.7) and PAN-01 (C30) fail. This indicates that strengthening bolt preload and increasing concrete strength grade can effectively improve the seismic performance of specimens, while excessively increasing the axial compression ratio will reduce the seismic performance of specimens.

4. Stress analysis

Since the main components of each node are the same, the stress cloud maps of each node have similar trends. A specific analysis will be conducted on the stress cloud maps of specimen PAN-07 (concrete grade C40; bolt preload 200kN; end-plate thickness 30mm; axial compression ratio 0.3) in the yield state, ultimate state, and failure state to correlate the node failure mechanism and seismic performance.

As shown in Fig. 9, the stress of the concrete column is evenly distributed from top to bottom by two sets of screw holes, and the force transmission path is clear, verifying the reasonable force transmission design of the through core bolt. In addition, the maximum stress around the screw hole and at the bottom of the column reaches 56.81 MPa, exceeding the design value of C40 concrete axial compressive strength (19.1 MPa). This indicates that this area is the starting point of failure of the concrete column. In the later stage of loading, compression first occurs, which is consistent with the failure of "column bottom concrete crushing" mentioned earlier.

As shown in Fig. 10, the stress of concrete beams is uniformly distributed outward from the upper and lower sides of the beam end. The maximum stress at the corner of the upper and lower ends of the beam end reaches 61.73 MPa, far exceeding the compressive strength threshold of C40 concrete. This area is the formation site of plastic hinges at the beam end. When it is loaded to the ultimate limit state, the concrete at the corner of the beam collapses first, causing the longitudinal reinforcement of the beam to lose lateral restraint, which in turn lead to the bending-type failure at the beam end. This is consistent with the failure mechanism of "fully developed plastic hinge at the beam end" mentioned earlier.

Table 6. Ductility coefficient of each specimen under different concrete strengths

Specimens		Yield load P_y/kN	Yield displacement Δ_y/mm	Ultimate load P_{max}/kN	Destruction displacement Δ_u/mm	Ductility coefficient μ
PAN-01	Positive	229.64	61.01	257.32	119.41	2.61
	Negative	-169.99	-52.44	-183.77	-147.46	2.81
PAN-02	Positive	182.46	41.61	192.58	144.23	3.47
	Negative	-181.62	-39.53	-190.64	-144.09	3.65
PAN-07	Positive	177.66	48.6	190.34	148.41	3.05
	Negative	-170.24	-40.63	-185.73	-148.65	3.66

Table 7. Ductility coefficient of each specimen under different pre tightening forces of bolts

Specimens		Yield load P_y/kN	Yield displacement Δ_y/mm	Ultimate load P_{max}/kN	Destruction displacement Δ_u/mm	Ductility coefficient μ
PAN-03	Positive	180.78	46.48	183.38	145.48	3.13
	Negative	-181.36	-45.46	-180.59	-149.95	3.30
PAN-04	Positive	178.84	39.49	180.56	146.87	3.72
	Negative	-183.81	-41.69	-182.51	-148.02	3.55
PAN-07	Positive	177.66	48.6	190.34	148.41	3.05
	Negative	-170.24	-40.63	-185.73	-148.65	3.66

Table 8. Ductility coefficient of each specimen under different end plate thicknesses

Specimens		Yield load P_y/kN	Yield displacement Δ_y/mm	Ultimate load P_{max}/kN	Destruction displacement Δ_u/mm	Ductility coefficient μ
PAN-05	Positive	142.94	35.83	171.38	149.09	4.16
	Negative	-158.11	-61.59	-165.02	-149.58	2.43
PAN-06	Positive	187.52	37.85	205.98	149.7	3.96
	Negative	-190.3	-36.86	-186.38	-145.67	3.95
PAN-07	Positive	177.66	48.6	190.34	148.41	3.05
	Negative	-170.24	-40.63	-185.73	-148.65	3.66

Table 9. Ductility coefficient of each specimen under different axial compression ratios

Specimens		Yield loadP_y/kN	Yield displacement Δ_y/mm	Ultimate loadP_{max}/kN	Destruction displacementΔ_u/mm	Ductility coefficient μ
PAN-07	Positive	177.66	48.6	190.34	148.41	3.05
	Negative	-170.24	-40.63	-185.73	-148.65	3.66
PAN-08	Positive	181.36	45.38	194.43	146.52	3.23
	Negative	-178.92	-37.81	-190.03	-147.91	3.91
PAN-09	Positive	188.78	40.15	218.83	149.5	3.72
	Negative	-185.07	-36.31	-214.01	-148.53	4.09

As shown in Fig. 11, the stress on the end plate is concentrated around the screw holes, with relatively smaller stress in the middle part (near the neutral axis). The upper and lower screw holes are symmetrically distributed, which conforms to the stress characteristics of bolted end plate connections. The maximum stress on the end plate reaches 350.8 MPa, approaching the yield strength of Q345 steel (345 MPa). After loading, the end plate only underwent slight deformation without failure, verifying the "strong node" design. The end plate dissipates energy through its own plastic deformation, preventing premature failure of the node.

As shown in Fig. 12, the stress of high-strength bolts is concentrated on both sides of the screw (close to the nut), and the stress distribution is uniform throughout the loading process. The force transmission effect is reliable, and the maximum stress of the bolt in the failure stage reaches 1082MPa, which is basically the same with the yield strength of the bolt (1080MPa). This indicates that the bolts have fulfilled its load-bearing function without slippage or fracture, ensuring the reliability of the node connection. This is the key guarantee in the design of "strong nodes".

As shown in Fig.13, the stress distribution is at the bottom of the steel cage column, and the stress distribution is relatively uniform in the entire loading stage, showing good force transmission effect. The maximum stress on the steel cage column reaches 474.1 MPa, exceeding the yield strength of the steel cage column and deforming slightly. The overall part does not suffer from large-scale damage.

As shown in Fig. 14, the maximum Mises stress of the concrete beam steel cage occurs at the junction between the concrete beam and the end plate and is mainly distributed on the upper and lower sides with g a symmetrical distribution. The main reason is that the concrete at the beam end is severely damaged, and the steel bars at the beam end gradually lose lateral support. When the specimen fails, it has exceeded the yield strength of the steel bars, indicating severe compression bending and bending failure, forming a typical plastic hinge failure mechanism at the beam end.

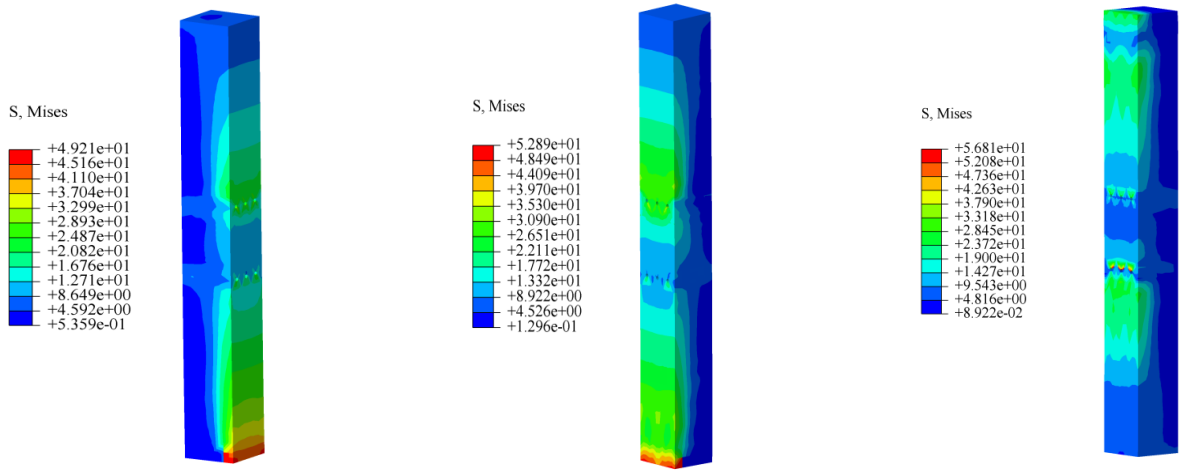

(a) Stress of column yield state (b) Stress of column ultimate state (c) Stress of column failure state

Fig. 9 Cloud diagram of stress stages in columns

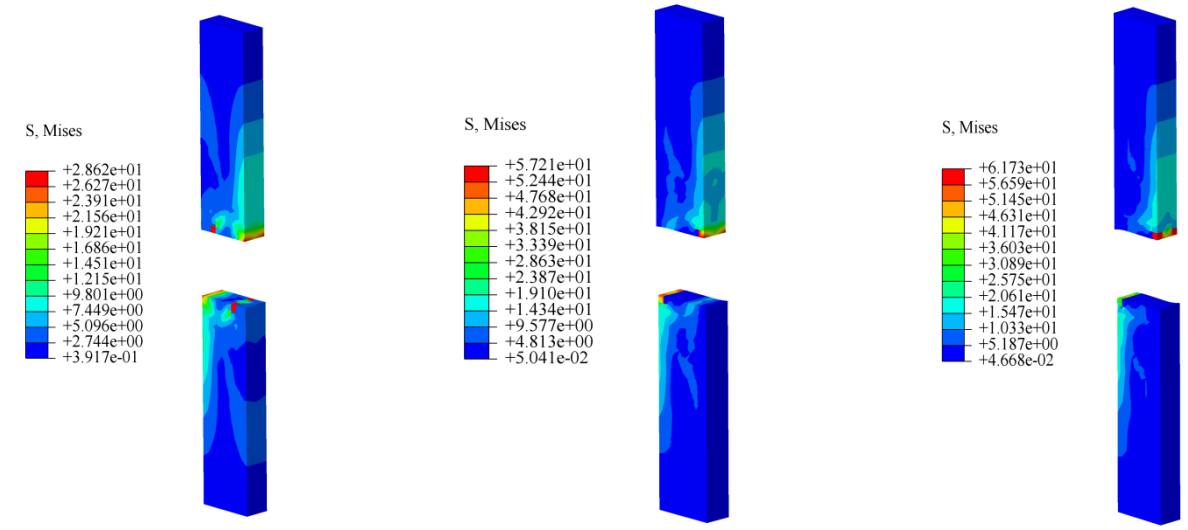

(a) Stress of beam yield state (b) Stress of beam ultimate state (c) Stress of beam failure state

Fig. 10 Cloud diagram of beam stress

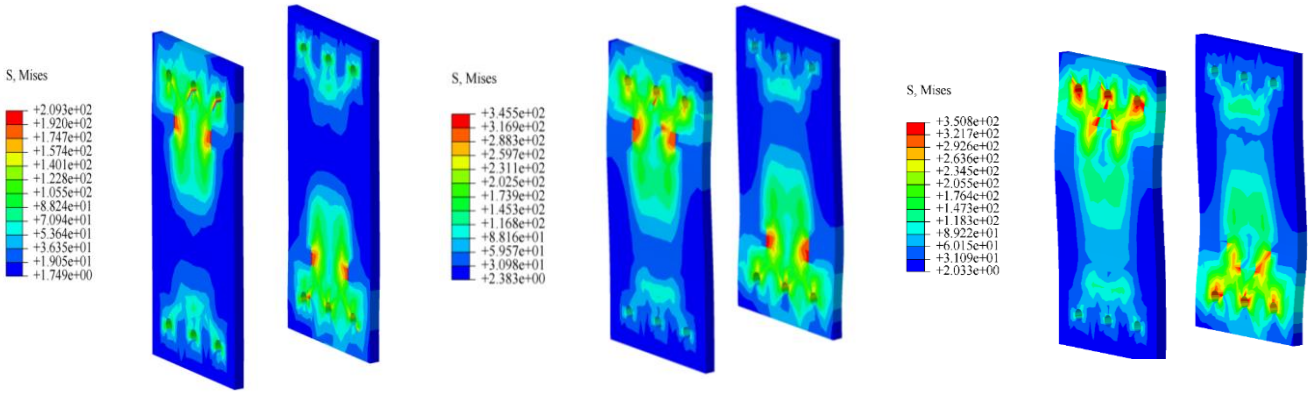

(a) Stress of end-plate yield state (b) Stress of end-plate limit state (c) Stress of end-plate failure state

Fig. 11 Cloud diagram of end-plate stress stage

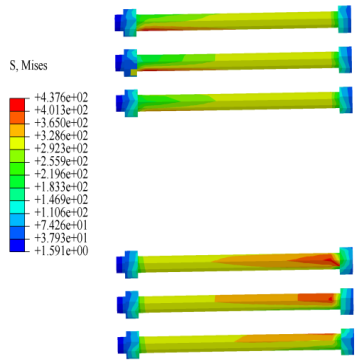

(a) Stress of yield state of high-strength bolts

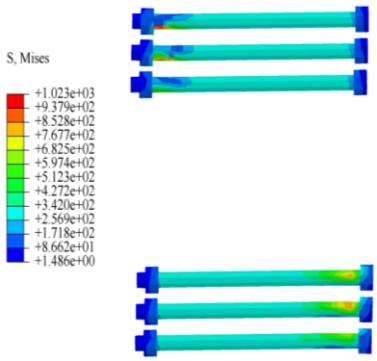

(b) Stress of ultimate state of high-strength bolts

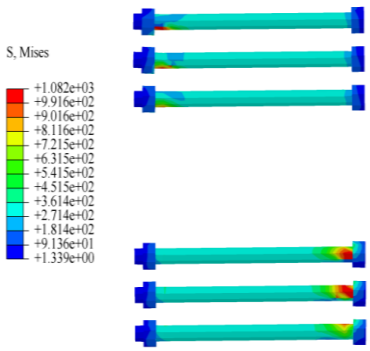

(c) Stress of failure state of high-strength bolt

Fig. 12 Cloud diagram of stress stages of high-strength bolts

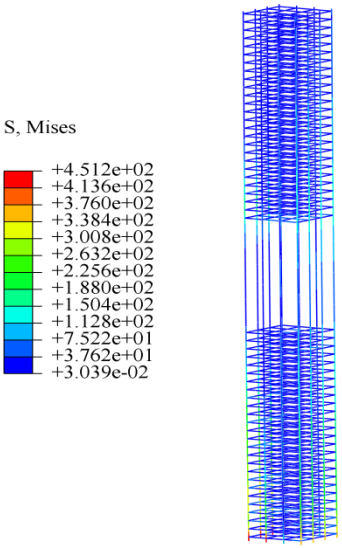

(a) Stress of yield state of column reinforcement cage

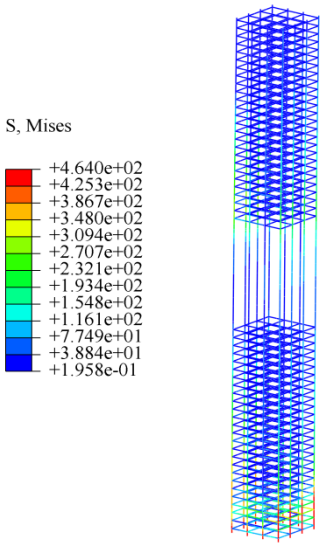

(b) Stress of ultimate state of column reinforcement cage

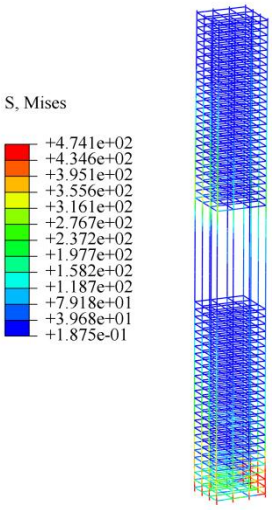

(c) Stress of column reinforcement cage failure state

Fig. 13 Cloud diagram of the stress of concrete beam reinforcement cage

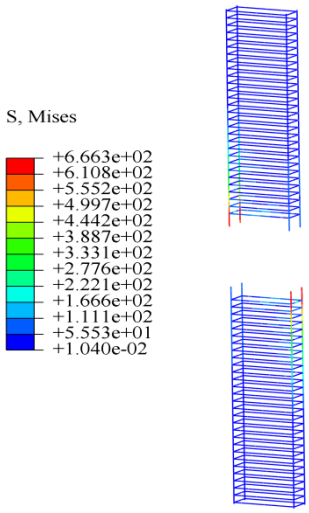

(a) Stress of yield state of beam reinforcement cage

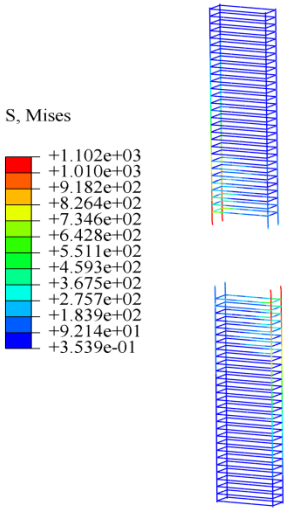

(b) Stress of ultimate state of beam reinforcement cage

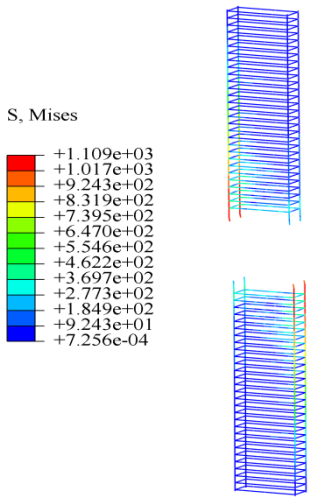

(c) Stress of beam reinforcement cage beam failure state

Fig. 14 Cloud diagram of the stress of concrete beam reinforcement cage

5. Conclusions

To study the seismic performance and failure mode of the structure, the finite element software is used to simulate low cycle repeated loading tests of the node. Axial compression ratio, concrete strength grade, end plate thickness, and other main variable parameters are modeled and analyzed. The influence of different influencing factors on the seismic performance of the node is explored, and main findings are drawn as follows:

(1) Compared with similar nodes, the advantages of the through core high-strength bolt connected prefabricated concrete frame nodes are significant: in terms of seismic performance, the component shows favorable hysteresis characteristics without significant pinching. It shows gradual stiffness degradation, and its ductility meets the requirements of RC structure design. In addition, the energy dissipation capacity is more significant than traditional composite nodes and bolted connection nodes. In construction, the connection methods is simple and do not require composite construction. This reduces the construction difficulty and cost, making post-earthquake maintenance convenient and more suitable for

the promotion of prefabricated buildings; At the level of force transmission and failure mechanism, a symmetrical design is used to achieve uniform stress distribution, avoid slip and local failure, fully develop the plastic hinge at the beam end, implement the "strong column, weak beam, stronger node" criterion, and meet the mainstream seismic design standards.

(2) Under the action of low cycle cyclic loading, the hysteresis curves of the 9 nodes exhibit similar characteristics, basically between shuttle shaped and bow shaped. The skeleton curves are basically the same, all experiencing four stages of elasticity, yield, strengthening, and decay. Under the same control displacement level, the three cycle curves are basically similar, and the degradation of strength and stiffness is not significant. The specimen exhibits good restoring force characteristics.

(3) The ductility coefficient of each node gradually increases as the parameter indicators improve. Node ductility coefficients range from 2.61 to 4.16, overall greater than 3.0. The equivalent viscous damping coefficient of the node specimen when it fails is 0.3 to 0.4, indicating that the node exhibits good ductility and energy dissipation capacity.

(4) Through comparing and analyzing the stress cloud diagrams of various components of the high-strength bolt connection assembled concrete frame node under different states, the stress of each component during the loading process can be clearly obtained. Overall, it can be seen that this type of structure can achieve the design criterion of "strong column, weak beam, stronger node", and the plastic hinge at the beam end can be fully developed, showing good deformation ability.

Acknowledgements

The work was supported by Henan Province's Department of Education under Grant No. 26B560018; Xuchang College Outstanding Young Backbone Teachers Funding Project; Henan Scientific and Technical Project under Grant No. 262102321083; Henan Province College Student Innovation Training Program under Grant No. S202510480048; Xuchang College Scientific Research Fund Project under Grant No. 2026YB059..

References

Al-Huri, M.A., Ahmad, S., Al-Osta, M., Al-Gadhib, A. H., Kharma, K. M. (2023) Performance of corroded RC beams strengthened in flexure using UHPC: Effect of configuration and thickness of the UHPC layers. Engineering Structures, vol. 292, pp. 116519. https://doi.org/10.1016/j.engstruct.2023.116519

Amer, M., Chen, Z., Du, Y., Kang, S., Mashrah, W.A.H. (2025) Experimental and numerical investigations on seismic behaviors of prefabricated composite CFT column V/Z-shaped truss. Journal of Constructional Steel Research, vol. 227, pp. 109364. https://doi.org/10.1016/j.jcsr.2025.109364

Bao, L., Han, X., Zhao, J., & Bao, Y. (2025) Seismic performance evaluation of precast bridge piers under combined freeze-thaw, chloride corrosion, and wetting-drying cycling effects. Structures, vol. 82, pp. 109899. https://doi.org/10.1016/j.istruc.2025.109899

Bao, L., Zhao, J., Teng, F., Bao, Y., Zhao, T., & Yu, L. (2023b) Experimental study on the seismic performance of prefabricated frame piers. Structures, vol. 52, pp. 651-665. https://doi.org/10.1016/j.istruc.2023.04.016

Bao, L., Zhao, J., Teng, F., Kong, Z., Yu, L., Bao, Y.,Yang, Y. (2023a) Experimental study on the seismic performance of precast segmental unbonded post-tensioned frame piers. Soil Dynamics and Earthquake Engineering, vol. 173, pp. 108143. https://doi.org/10.1016/j.soildyn.2023.108143

Elflah, M., Theofanous, M., Dirar, S., Yuan, H.X. (2019a) Behaviour of stainless steel beam-to-column joints-Part 1: Experimental investigation. Journal of Constructional Steel Research. vol. 152, pp. 183-193. https://doi.org/10.1016/j.jcsr.2018.02.040

Elflah, M., Theofanous, M., Dirar, S., Yuan. H. (2019b) Structural behaviour of stainless steel beam-to-tubular column joints. Engineering Structures, vol. 184, pp. 158-175. https://doi.org/10.1016/j.engstruct.2019.01.073

Fang, Z.H., Zheng, Y., Li, X.P. (2018) Steel hysteretic model of reinforced concrete structures (In Chinese). Engineering Journal of Wuhan University, vol. 51, no. 7, pp. 613-619. https://doi.org/10.14188/j.1671-8844.2018-07-008

GB50010-2010 (2010) Code for Design of Concrete Structures (In Chinese). China Architecture and Building Press, Beijing.

Hassan, A.S.B.Z., Algobahi, R.M., Fahmy. M. F. M. (2024) Post-tensioned steel beam-column connections with reduced length BFRP tendons. Journal of Constructional Steel Research, vol. 214, pp. 108423. https://doi.org/10.1016/j.jcsr.2023.108423

Kalmykova, S. (2021) Simulation of T-Joints between RHS Steel Members with Offset in Abaqus. Acta Polytechnica CTU Proceedings, vol.30, pp. 36-40. https://doi.org/10.14311/APP.2021.30.0036

Nejati, F., Kiaie, M.M., Edalatpanah, S.A. (2019) A Numerical Modelling for Seismic Behavior of Frames with CFST Composite Columns and Torsional Semi-Rigid Connection. American Journal of Civil Engineering and Architecture, vol. 7, no. 2, pp. 52-60. https://doi.org/10.12691/AJCEA-7-2-2

Nzabonimpa, J.D., Hong, W.K., Kim, J. (2018) Experimental and non-linear numerical investigation of the novel detachable mechanical joints with laminated plates for composite precast beam-column joint. Composite Structures, vol. 185, pp. 286-303. https://doi.org/10.1016/j.compstruct.2017.11.024

Rahnavard, R., Rebelo, C., Craveiro, H.D., Napolitano, R. (2020) Numerical investigation of the cyclic performance of reinforced concrete frames equipped with a combination of a rubber core and a U-shaped metallic damper. Engineering Structures, vol. 225, pp. 111307, https://doi.org/10.1016/j.engstruct.2020.111307

Ramseyer, C., Sherry, S. T. (2019) Assessment of partial joint penetration welds on bolted end-plate connections. Engineering Structures, vol. 197, pp. 09400. https://doi.org/10.1016/j.engstruct.2019.109400

Tekieh, S. M. R., Zandi, A. P., Pashaei, M. H. (2022) Numerical and experimental study of the BUEEP connection using an inner box. Journal of Constructional Steel Research, vol.193, pp. 107264. https://doi.org/10.1016/j.jcsr.2022.107264

Wu, C., Liu, J. & Shi, W. (2020b) Seismic performance of composite joints between prefabricated steel-reinforced concrete columns and steel beams: experimental study. Bulletin of Earthquake Engineering, vol. 18, pp. 3817-3841. https://doi.org/10.1007/s10518-020-00842-y

Wu, C., Yu, S., Liu, J., Chen, G. (2020a) Development and testing of hybrid precast steel-reinforced concrete column-to-H shape steel beam connections under cyclic loading. Engineering Structures, vol. 211, pp. 110460. https://doi.org/10.1016/j.engstruct.2020.110460

Wu, D., Li, W., Chen, Y.Z., Xu, C., Li, C. (2022) Seismic performance of steel beam to concrete-filled steel tubular column Bolted edge column joint with outside ring plates(In Chinese). Journal of Civil Engineering and Management, vol. 39, no. 1, pp.75-79. https://doi.org/10.13579/j.cnki.2095-0985.2022.0106.001

Yeganeh, A.E., Hossain, K.M.A. (2023) Structural behavior of shear deficient high performance reinforced concrete exterior joints under bending. Structures, vol. 48, pp. 1707-1721. https://doi.org/10.1016/j.istruc.2023.01.064

Zhang, F.R., Xu, Q., Jiang, P., Zhu, Y., Li, X. (2020) Study on hysteretic behavior of new steel beam to concrete-filled Square steel tubular column joint with double T-stub-bidirectional bolts(In Chinese). Journal of Xi'an University of Architecture & Technology (Natural Science Edition), vol. 52, no. 1, pp. 54-62. https://doi.org/10.15986/j.1006-7930.2020.01.008

Zhelyazov, T., Thorhallsson E. (2022) Analytical and Numerical Approaches for the Design of Concrete Structural Elements with Internal BFRP Reinforcement.Materials (Basel, Switzerland), vol.15, no. 4, pp. 1497. https://doi.org/10.3390/ma15041497

Disclaimer